Single-Satellite Doppler-Based Localization for Lunar Rovers in Motion

Kaila M. Y. Coimbra and Grace Gao
Stanford University

Kaila M. Y. Coimbra is a Ph.D. candidate in the Department of Aeronautics and Astronautics at Stanford University. She received her B.S. in Mechanical Engineering, with a minor in Aerospace Engineering, from the California Institute of Technology. Her research interests include positioning, navigation, and timing, particularly for lunar surface rovers.

Grace Gao is an associate professor in the Department of Aeronautics and Astronautics at Stanford University. She leads the Navigation and Autonomous Vehicles Laboratory (NAV Lab). Before joining Stanford University, she was an assistant professor at the University of Illinois at Urbana-Champaign. She obtained her Ph.D. degree at Stanford University. Her research is on robust and secure positioning, navigation, and timing with applications to manned and unmanned aerial vehicles, autonomous driving cars, as well as space robotics.

ABSTRACT

Early lunar rovers will likely operate before a dedicated lunar navigation constellation is in place, making single-satellite relay links the most practical source of navigation signals for these early-stage rovers. In this work, we study the absolute localization performance using Doppler measurements from a single relay satellite while the rover is moving–a setting that challenges traditional navigation methods due to its intrinsically low observability. Our approach uses the rover's own motion knowledge (dead reckoning with uncertainty) to relate measurements taken at different times, thereby aggregating multiple geometric viewpoints of the rover's position through successive satellite passes. We formulate a weighted batch estimator that retains the full measurement history and models conservative uncertainties while treating rover motion as a standard Dubins car kinematic model. Validation is performed in a mission-realistic scenario patterned after NASA's Endurance rover mission concept and ESA's Lunar Pathfinder relay satellite in an elliptical lunar frozen orbit. We find that the stop–go mission cadence, which is already required for science imaging and sampling, shortens the time to achieve the desired accuracy by nearly an hour in our study. A sensitivity analysis shows that the system maintains sub-10-m accuracy within two relay orbits (21.68 hours). These results indicate that planned operational dynamics can be leveraged, not merely tolerated, to enable absolute localization for early lunar rovers using a single relay satellite.

I. INTRODUCTION

Recent advances in technology, international collaboration, and industry partnerships have re-ignited a global interest in lunar exploration. Within the next five years, we are expected to see a surge in lunar surface rover missions, including the NASA CADRE robots (Rabideau et al., 2025), Astrolab's FLEX rover (Astrolab Venturi, 2025), the JAXA/ISRO LUPEX rover (Mizuno et al., 2024), and the NASA Endurance rover (Keane et al., 2022). Accurate and precise localization of lunar rovers is essential to each mission because the lunar terrain can be difficult to traverse, leading to potential immobilization, and sample-collection rovers must geotag samples with high accuracy to fulfill science objectives. Many space agencies are proposing several lunar constellations to provide navigation and communication services to lunar assets. In particular, the LunaNet constellation, which will consist of NASA's Lunar Communication Relay and Navigation System (LCRNS), ESA's Moonlight, and JAXA's Lunar Navigation Satellite System (LNSS), will be an international effort to create a GNSS-like system around the Moon (Giordano et al., 2023).

Despite these efforts, the timeline for deployment of a navigation constellation system does not align with the expected timeline for some early-stage lunar rover missions. The NASA Endurance rover, which was identified by the Planetary Science and Astrobiology Decadal Survey as a critical mission to achieve "transformative science" on the Moon (National Academies of Sciences, Engineering, and Medicine, 2023), will need to localize itself without relying on a full lunar constellation. A satellite that is expected to be operational and available to early-stage surface rover missions is the pilot satellite from ESA's Moonlight constellation—the Lunar Pathfinder (SSTL, 2022). Based on current plans, the Lunar Pathfinder will only be able to provide communication services, meaning that any navigation observables from the satellite will have to be opportunistically extracted from the signal's Doppler shift. While localization methods using a rover's onboard sensors exist, no approach has yet integrated measurements from a single relay satellite to enhance the positioning accuracy for early-stage lunar rovers in motion.

Previous works, specific to the Endurance mission, have investigated the localization accuracy of the rover using only vision-based methods through autonomous crater detection and matching (Daftry et al., 2023; Cauligi et al., 2023). Although these

vision-based methods demonstrate a desirable localization error of less than $10\ \mathrm{m}$, they depend on factors that are difficult to guarantee operationally, such as high-quality onboard maps, sufficient and distinguishable surface features, and favorable illumination.

Other localization methods include exploiting weak signals from terrestrial GPS, which was recently demonstrated by the Lunar GNSS Receiver Experiment (LuGRE) in March 2025 (Parker et al., 2025). However, weak GPS does not provide coverage at the lunar South Pole, which is the region of principal scientific interest for upcoming rover missions (Keane et al., 2022). A complementary approach employs relay-assisted techniques for localization. In particular, Joint Doppler and Ranging uses geometric constraints from Doppler shift measurements to estimate the user's position with respect to a lunar reference station (Jun, 2023). Although promising, this approach assumes infrastructure that exceeds the capabilities expected for early missions, and thus is misaligned with the minimal-infrastructure context considered in this work.

Our previous study investigated the localization accuracy attainable using only Doppler measurements from ESA's Lunar Pathfinder, which is consistent with anticipated mission resources (Coimbra et al., 2024). The proposed estimator accumulates measurements over time, which is equivalent to obtaining measurements from multiple virtual satellites. Due to limited observability in the single-satellite geometry, the estimator required the rover to remain stationary for a mean of 11.2 hours to reduce the position error below $10\ \mathrm{m}$. Requiring the rover to be stationary for several hours places a heavy operational burden. This motivates the present question: can comparably accurate absolute localization be achieved while the rover is in motion by leveraging its onboard dead-reckoning capability?

1. Proposed Approach

We extend our prior work by analyzing single-satellite localization during moving operations. The central assumption is that the rover possesses usable motion knowledge. In other words, the rover knows, with some uncertainty, its displacement from a global start via dead reckoning—even if its absolute pose is initially biased. The stationary assumption (known constant pose) is functionally equivalent here to a known dead-reckoned displacement from a fixed anchor, allowing us to apply the same temporal 'virtual satellite' construction as in the stationary case.

We design a weighted batch filter that precomputes the relative displacements from the start and minimizes the measurement residual over a growing batch of measurements. The measurement model accounts for thermal, receiver-clock, and ephemeris errors; rover motion follows a Dubins car kinematic model. For validation, we instantiate a mission-realistic scenario using NASA's Endurance rover mission concept (Keane et al., 2022) and ESA's Lunar Pathfinder relay satellite (SSTL, 2022).

2. Key Contributions

The new and innovative aspects of the paper are described below:

- To the best of the authors' knowledge, this paper is the first to develop a localization filter for a moving lunar rover using measurements from a single satellite without a dedicated navigation payload.
- We simulate a scheduled mission cadence based on a planned long-duration rover traverse to validate our filter design.
- We quantify the filter's tolerance to injected noise in the rover's velocity while maintaining the desired localization accuracy.

II. STATE ESTIMATION ALGORITHM

We employ a weighted batch filter to refine the rover state from pseudorange rate measurements. A batch filter approach is preferred over recursive filters, such as the Extended Kalman Filter (EKF), because it retains the full measurement history, which is essential in low-observability settings such as the single-satellite case. This section presents the weighted batch filter formulation used for moving rovers, including the construction of the weighting matrix and the treatment of measurement and modeling uncertainties.

1. Weighted Batch Filter

The filter solves for the rover's 3D position and clock drift. Clock bias is not observable from pseudorange-rate (Doppler) alone. We intentionally exclude rover velocity from the state to avoid over-parameterizing an already low-observability single-satellite geometry. Thus, we define the rover's position $\mathbf{r}_{\boldsymbol{r},k}$ and state $\mathbf{x}_{\boldsymbol{r},k}$ as follows.

$$\mathbf{r}_{\boldsymbol{r},k} = \begin{bmatrix} x_k & y_k & z_k \end{bmatrix}^\top \tag{1}$$

$$\mathbf{x}_{\boldsymbol{r},k} = \begin{bmatrix} \mathbf{r}_{\boldsymbol{r},k} & c \cdot \dot{\delta t}_{r,k} \end{bmatrix}^\top \tag{2}$$

Rather than estimating velocity directly, we utilize the rover's knowledge of its motion (i.e., through the rover's onboard inertial measurement unit (IMU), LiDAR, or wheel odometry) to supply a relative displacement between the global start and each epoch. In effect, the filter trades explicit velocity states for a set of relative-motion pseudo-observations, which better exploits available onboard information. The details of the relative position accuracy are outside the scope of this study, but an analysis on the sensitivity to injected velocity noise is reported in Section V.4.

At time step N, the rover stacks its previously observed pseudorange rate measurements $\tilde{\dot{\boldsymbol{\rho}}}$ as shown in Equation 3.

$$\tilde{\dot{\boldsymbol{\rho}}} = \begin{bmatrix} \tilde{\dot{\rho}}(t_1) & \dots & \tilde{\dot{\rho}}(t_N) \end{bmatrix}^\top \tag{3}$$

Likewise, the rover predicts its expected pseudorange rate measurements $\hat{\dot{\boldsymbol{\rho}}}_{k+1}$ given its erroneous initial position and the precomputed relative displacements.

$$\hat{\dot{\boldsymbol{\rho}}}_{k+1} = \begin{bmatrix} \hat{\dot{\rho}}_{k+1}(t_1) & \dots & \hat{\dot{\rho}}_{k+1}(t_N) \end{bmatrix}^\top \tag{4}$$

To update the rover state, the filter minimizes the following cost function, which is the weighted Euclidean norm of the measurement residual.

$$C = \|\tilde{\dot{\boldsymbol{\rho}}} - \hat{\dot{\boldsymbol{\rho}}}_{k+1}\|^2_{\mathbf{W}} \tag{5}$$

We obtain the Gauss-Newton step by performing a first-order linearization of the predicted measurement model about the iterate $\mathbf{x}_{\boldsymbol{r},k}$, where $\mathbf{J}_k$ is the measurement Jacobian matrix.

$$\delta\mathbf{x}_k = \left(\mathbf{J}_k^\top \mathbf{W} \mathbf{J}_k\right)^{-1} \mathbf{J}_k^\top \mathbf{W} \delta\mathbf{y}_k \tag{6}$$

Inclusion of the weighting matrix $\mathbf{W}$ improves the filter performance by capturing the anticipated uncertainty at each epoch.

$$\mathbf{W} = \operatorname{diag}\left(\sigma_{tot}^{-2}(t_1)\ ,\ \dots\ ,\ \sigma_{tot}^{-2}(t_N)\right) \tag{7}$$

$$\sigma_{tot}^2 = \sigma_t^2 + \sigma_c^2 + \sigma_e^2 + \sigma_s^2 \tag{8}$$

Here, σ_t^2, σ_c^2, and σ_e^2 denote the thermal, clock, and ephemeris noise contributions, respectively. Sections III.4 and III.5 define these noise profiles in more depth. The term σ_s^2 represents rover motion uncertainty and is discussed in Section III.6 b). In principle, σ_s^2 should be scaled by the line-of-sight projection of the rover's velocity. However, we adopt a conservative upper bound (without projection), which yielded better performance in simulation. The state is updated iteratively as follows until convergence.

$$\hat{\mathbf{x}}_{\boldsymbol{r},k+1} = \hat{\mathbf{x}}_{\boldsymbol{r},k} + \delta\mathbf{x}_k \tag{9}$$

After each update, the filter re-propagates to the current epoch while the initial position serves as a fixed anchor, allowing the batch to grow in time while exploiting all past measurements.

III. MODELING

1. Observed Measurement Model

When using a single satellite without a navigation payload, we must opportunistically extract the navigation observable by calculating the Doppler shift of the communication signal. The Doppler shift is the change in frequency from the source to the receiver caused by the relative motion between the satellite and the rover. Equivalently, pseudorange rate $\dot{\rho}$ is a scalar multiple of Doppler shift D as seen in Equation 10, where c is the speed of light and f is the frequency of the communication signal.

$$\dot{\rho} = -\frac{Dc}{f} \tag{10}$$

In simulation, we can generate observed pseudorange rate measurements $\tilde{\dot{\rho}}$ through Equation 11. The first term in Equation 11 is the true range rate (the projection of the relative velocity onto the line of sight vector between the rover and the satellite). The

pseudorange rate includes added contributions of the relative clock drift and the measurement noise.

$$\tilde{\dot{\rho}}(t) = (\mathbf{v_s} - \mathbf{v_r}) \cdot \frac{\mathbf{r_s} - \mathbf{r_r}}{\|\mathbf{r_s} - \mathbf{r_r}\|} + c\left(\dot{\delta}t_r - \dot{\delta}t_s\right) + \varepsilon_{\dot{\rho}} \tag{11}$$

According to O'Dea et al. (2019), thermal noise at the receiver and the clock noise at the source and the receiver are the main contributors to the measurement error. Thus, in this work, we model the measurement noise as a zero-mean white Gaussian noise with a variance $\sigma_{\dot{\rho}}^2$ that is the sum of the thermal noise variance σ_t^2 and clock noise variance σ_c^2. The definitions for the thermal and clock variances can be found in Section III.4.

$$\varepsilon_{\dot{\rho}} \sim \mathcal{N}(0, \sigma_{\dot{\rho}}^2) \quad , \quad \sigma_{\dot{\rho}}^2 = \sigma_t^2 + \sigma_c^2 \tag{12}$$

2. Predicted Measurement Model

In the state estimation filter described in Section II, we minimize the residual, which is the difference between the observed and the predicted measurements. The predicted pseudorange rate $\hat{\dot{\rho}}_{k+1}$ follows a similar model as to the observed pseudorange rate in Equation 11.

$$\hat{\dot{\rho}}_{k+1} = (\tilde{\mathbf{v}}_{\boldsymbol{s}} - \hat{\mathbf{v}}_{\boldsymbol{r},k+1}) \cdot \frac{\tilde{\mathbf{r}}_{\boldsymbol{s}} - \hat{\mathbf{r}}_{\boldsymbol{r},k+1}}{\|\tilde{\mathbf{r}}_{\boldsymbol{s}} - \hat{\mathbf{r}}_{\boldsymbol{r},k+1}\|} + c\left(\hat{\dot{\delta}}t_{r,k+1} - \dot{\delta}t_s\right) \tag{13}$$

First, the rover predicts its range rate based on its erroneous knowledge of the satellite's position $\tilde{\mathbf{r}}_{\boldsymbol{s}}$ and velocity $\tilde{\mathbf{v}}_{\boldsymbol{s}}$ and its current state estimate as denoted by $\hat{\mathbf{r}}_{\boldsymbol{r},k+1}$ and $\hat{\mathbf{v}}_{\boldsymbol{r},k+1}$. Then, the relative clock drift term is added using the rover's current estimate of its clock drift $\hat{\dot{\delta}}t_{r,k+1}$.

3. Communication Signal Model

The signal quality at the receiver can be quantified through the carrier-to-noise density ratio C/N_0. The received C/N_0 is a sum of the isometric power P_r, the gain-to-noise temperature ratio g/T, and the Boltzmann constant k_B.

$$C/N_0 = P_r + g/T - k_B \tag{14}$$

For more information on our model for the received isometric power P_r and the receiver's gain-to-noise temperature ratio g/T, refer to Coimbra et al. (2024). The carrier-to-noise density ratio C/N_0 is used to define the thermal noise variance σ_t^2 (see Section III.4 a) and is also a parameter used to define signal availability (see Section V.1).

4. Measurement Error Model

a) Thermal Noise

Following O'Dea et al. (2019), we model the thermal noise variance σ_t^2 with Equation 15, where B_L is the bandwidth of the downlink carrier loop, S_L is the squaring loss of the Costas loop, and T is the integration time.

$$\sigma_t^2 = \frac{2B_L}{C/N_0 \cdot S_L}\left(\frac{c}{2\pi f T}\right)^2 \tag{15}$$

O'Dea et al. (2019) and Coimbra and Gao (2025) provide more information on how to calculate the squaring loss of the Costas loop S_L.

b) Clock Noise

Similarly, we model the clock noise error with the model in O'Dea et al. (2019) such that the error is the scaled sum of the Allan variances of the satellite and rover's clock, as shown in Equation 16.

$$\sigma_c^2 \simeq c^2\left(\sigma_{c,s}^2 + \sigma_{c,r}^2\right) \tag{16}$$

The Allan variance is equivalent to the variance in the fractional frequency q_{22} as found in the clock process noise covariance matrix $\mathbf{Q}$. The fractional frequency variance q_{22} is a function of the clock's power spectral density (PSD) coefficients–h_0, h_{-1},

and h_{-2}–and the measurement sampling time τ. The PSD coefficients used for the satellite and rover clocks are specified in Section IV.

$$\mathbf{Q} = \begin{bmatrix} q_{11} & q_{12} \\ q_{21} & q_{22} \end{bmatrix}, \tag{17}$$

$$q_{11} = \frac{\tau}{2} h_0 + 2\tau^2 h_{-1} + \frac{2\pi^2 \tau^3}{3} h_{-2}, \tag{18}$$

$$q_{12} = q_{21} = \tau h_{-1} + \pi^2 \tau^2 h_{-2}, \tag{19}$$

$$q_{22} = \frac{1}{2\tau} h_0 + 4h_{-1} + \frac{8\pi^2 \tau}{3} h_{-2} \tag{20}$$

5. Ephemeris Noise Model

To model ephemeris noise, we apply a zero-mean white Gaussian noise term to the satellite's position $\tilde{\mathbf{r}}_{\boldsymbol{s}}$ and velocity $\tilde{\mathbf{v}}_{\boldsymbol{s}}$.

$$\tilde{\mathbf{r}}_{\boldsymbol{s}} = \mathbf{r}_{\boldsymbol{s}} + \boldsymbol{\varepsilon}_{\boldsymbol{e,p}} \quad , \quad \boldsymbol{\varepsilon}_{\boldsymbol{e,p}} \sim \mathcal{N}(\mathbf{0}_{3\times3}, \sigma^2_{e,p_{xyz}} \mathbf{I}_{3\times3}) \tag{21}$$

$$\tilde{\mathbf{v}}_{\boldsymbol{s}} = \mathbf{v}_{\boldsymbol{s}} + \boldsymbol{\varepsilon}_{\boldsymbol{e,v}} \quad , \quad \boldsymbol{\varepsilon}_{\boldsymbol{e,v}} \sim \mathcal{N}(\mathbf{0}_{3\times3}, \sigma^2_{e,v_{xyz}} \mathbf{I}_{3\times3}) \tag{22}$$

Note that the ephemeris noise is applied only to the predicted pseudorange rate model, as the rover will have erroneous knowledge of the satellite state. Thus, the ephemeris noise is not captured in the measurement error, but is considered by the filter through the weighting matrix $\mathbf{W}$ as shown in Equations 7 and 8.

While we recognize that a white-noise ephemeris error is conservative and non-systematic, we adopt it here because the satellite ephemeris update cadence has not yet been publicly specified. As future work, we will increase model fidelity by treating ephemeris errors as a time-correlated process (e.g., random walk or Gauss–Markov).

6. Rover Motion Model

We model the Moon as a smooth sphere with a radius R_M of 1737.4 km. For straight-line motion, the rover is assumed to follow a great-circle geodesic (i.e., the largest possible circle on the sphere). Rover kinematics are represented by the standard Dubins car model.

a) Dubins Car Model

The rover state is (ϕ, λ, θ, s), where ϕ and λ are the rover's latitude and longitude coordinates, θ is the heading in the local East-North-Up (ENU) reference frame, and s is the ground speed. The control input is (ω, a), comprising the heading rate and acceleration, respectively. The ground velocity components in the local ENU frame are as follows.

$$v_E = s \cos\theta \tag{23}$$

$$v_N = s \sin\theta \tag{24}$$

We can propagate the rover's state using spherical kinematics.

$$\dot{\phi} = \frac{v_N}{R_M} \tag{25}$$

$$\dot{\lambda} = \frac{v_E}{R_M \cos\phi} \tag{26}$$

$$\dot{\theta} = \omega \tag{27}$$

$$\dot{s} = a \tag{28}$$

Since the satellite ephemerides are expressed in the Moon Principal Axis (PA) frame, rover states computed in the local ENU frame are mapped to the Moon PA frame before measurement modeling. The rover position in the Moon PA frame is

$$\mathbf{r}_{\boldsymbol{r}} = R_M \begin{bmatrix} \cos\phi\cos\lambda \\ \cos\phi\sin\lambda \\ \sin\phi \end{bmatrix} \tag{29}$$

By computing the time derivative of Equation 29, we can also compute the rover's velocity in the Moon PA frame.

$$\mathbf{v}_{\boldsymbol{r}} = \frac{d\mathbf{r}_{\boldsymbol{r}}}{dt} = \frac{\partial \mathbf{r}_{\boldsymbol{r}}}{\partial \phi}\dot{\phi} + \frac{\partial \mathbf{r}_{\boldsymbol{r}}}{\partial \lambda}\dot{\lambda} \tag{30}$$

$$\mathbf{v}_{\boldsymbol{r}} = R_M \begin{bmatrix} -\sin\phi\dot{\phi}\cos\lambda - \cos\phi\sin\lambda\dot{\lambda} \\ -\sin\phi\dot{\phi}\sin\lambda + \cos\phi\cos\lambda\dot{\lambda} \\ \cos\phi\dot{\phi} \end{bmatrix} \tag{31}$$

b) Velocity Noise

To account for wheel slip and other traversal effects, we perturb the rover's ground–truth speed with zero–mean white Gaussian noise.

$$\tilde{s} = s + \varepsilon_s \quad , \quad \varepsilon_s \sim \mathcal{N}(0, \sigma_s^2) \tag{32}$$

This perturbation is applied only in the truth model; the filter propagation uses a noise-free motion model. The resulting speed variance is represented in the filter through the weighting matrix $\mathbf{W}$ (see Equations 7–8). We assume accurate heading from onboard star trackers and Sun sensors, so no heading noise is injected.

IV. VALIDATION

1. Endurance Mission Concept

We validate our approach in the context of NASA's Endurance rover mission concept because it represents a particularly demanding and operationally relevant use case. The rover is planned to autonomously traverse $2000\ \mathrm{km}$ in the lunar South Pole region with frequent sampling along its route (Keane et al., 2022). Such a mission demands high-accuracy absolute localization to geotag samples over long traverses. The traverse scale and lunar environment also limit the opportunities for ground support, such as a lunar ground station.

a) Relevant Hardware Components

The planned communications payload of the Endurance rover includes a $75\ \mathrm{cm}$ high-gain omnidirectional antenna, and we assume that the antenna is continuously steered toward the relay satellite. Per the Endurance specifications, the antenna can maintain a lock with an effective gain of $22.0\ \mathrm{dB}$ while preserving a 3° pointing margin (Keane et al., 2022).

Thermal noise at the receiver is defined in Section III.4 a). We set the downlink carrier loop bandwidth B_L to be $1\ \mathrm{Hz}$ and the integration time T to be $0.02\ \mathrm{s}$. Under these settings, the resulting thermal noise spans roughly from 10^{-1} to $10^{1}\ \mathrm{mm/s}$ as a function of the carrier-to-noise density ratio C/N_0.

To the best of the authors' knowledge, the specifications for the rover's onboard clock have not been publicly released. Building on our prior sensitivity analysis, which identified the Stanford Research Systems (SRS) PRS 10 clock as mission-appropriate (Coimbra et al., 2024), we assume the rover carries an SRS PRS 10 clock. Table 1 summarizes its size, weight, and power consumption (SWaP) characteristics, the PSD coefficients, and the resulting time deviation per day.

Table 1: Clock parameters (Schmittberger and Scherer, 2020; Bhamidipati et al., 2022)

Parameter	SRS PRS 10	Excelitas RAFS
Size [cm^3]	155	1645
Weight [kg]	0.6	6.35
Power [W]	14.4	39
TDEV per day [µs]	7.0×10^{-2}	4.8×10^{-3}
h_0 [Hz^{-1}]	1.3×10^{-22}	8.0×10^{-27}
h_{-1}	2.3×10^{-26}	–
h_{-2} [Hz]	3.3×10^{-31}	–

b) Rover Motion Profile

Due to the low observability of the single-satellite architecture, the localization accuracy varies strongly with the rover's location on the Moon. To focus the analysis, we fix the rover's initial position at the Poincaré Q waypoint (59.12448° S, 161.05104° E), which is a site of high scientific interest within the South Pole-Aitken basin. The Endurance mission includes two candidate $2000\ \mathrm{km}$ traverse routes that both pass through the Poincaré Q waypoint, indicating its scientific and exploration relevance for our study.

In this study, we evaluate two straight-line rover motion profiles: (1) constant speed and (2) stop-go. The Endurance rover is expected to have an average traverse speed of $0.5\ \mathrm{km/hr}$, or $0.14\ \mathrm{m/s}$. The constant-speed motion profile simply applies this average traverse speed throughout the simulation. To reflect the planned mission profile, the stop-go schedule is parameterized from the Endurance mission concept. For nominal operations during the lunar day, the rover stops every $300\ \mathrm{m}$ for 10 minutes to image its surroundings and, in addition, every $2\ \mathrm{km}$ for a 1 hour extended stop to collect samples. This stop-go cycle repeats for the duration of the simulation.

2. Lunar Pathfinder

We adopt ESA's Lunar Pathfinder as the relay satellite because it is planned for near-term deployment (targeted for 2026), making it representative of the infrastructure likely to be available during early-stage surface missions such as Endurance (SSTL, 2022).

a) Orbit

The Lunar Pathfinder satellite operates in an elliptical lunar frozen orbit (ELFO) with orbital elements summarized in Table 2; the orbital period is $10.84\ \mathrm{hours}$ (SSTL, 2022). ELFOs offer several mission-relevant advantages: (1) offer long-term dynamical stability with minimal station-keeping, (2) produce a ground track that precesses, so the line-of-sight geometry evolves slowly over a lunar month, and (3) provide sustained visibility of the South Pole region, which is the focus area for early lunar rover missions.

Table 2: The Lunar Pathfinder's Keplerian orbital elements and orbital period (SSTL, 2022)

Parameter	Value
Semi-major axis [km]	5740
Eccentricity	0.58
Inclination [°]	54.856
Right Ascension of the Ascending Node (RAAN) [°]	0
Argument of the Periapsis [°]	86.322
Mean Anomaly [°]	80
Orbital Period [hr]	10.84

b) Communication Signal and Transmitter Antenna

The Lunar Pathfinder is designed to support lunar assets over S-band and Ultra-High Frequency (UHF), with an X-band link for relay to Earth (SSTL, 2022). Because Endurance-class rovers nominally use S-band (Keane et al., 2022), we model the downlink within the specified 2025 to $2110\ \mathrm{MHz}$ allocation and adopt a representative carrier of $2050\ \mathrm{MHz}$. The waveform assumes convolutional coding at rate $r = 1/2$ with binary phase-shift keying (BPSK) modulation.

Per the Endurance mission specifications, the effective isotropic radiated power (EIRP) available to surface users spans roughly 12 to $26.5\ \mathrm{dB\,W}$, and the S-band downlink exceeds $20.14\ \mathrm{dB\,W}$ at the 7.1° half-power beamwidth (HPBW) (Keane et al., 2022). In our model, the transmitter is a parabolic antenna with $26.5\ \mathrm{dB\,W}$ at boresight and HPBW of 7.1°. Off-boresight gain is computed from this pattern under a nadir-pointing assumption (i.e., the spacecraft points toward the lunar center). Table 3 summarizes the parameters for the communication signal and the transmitter antenna.

c) Clock

We assume that the Lunar Pathfinder is equipped with the Excelitas RAFS clock, which is a higher fidelity clock compared to the rover's SRS PRS 10 clock. The clock parameters for the Excelitas RAFS are provided in Table 1. Although the size and weight of the Excelitas RAFS are an order of magnitude larger than that of the SRS PRS 10, the PSD coefficients are several orders of magnitude more stable. In fact, the flicker frequency modulation (FM) h_{-1} and random walk FM h_{-2} are considered negligible for the Excelitas RAFS.

Table 3: Communication signal and transmitter antenna parameters

Parameter	Value
S-band downlink frequency f [MHz]	2050
Coding rate r	0.5
EIRP at boresight [dB W]	26.5
HPBW [°]	7.1

d) Ephemeris Errors

SSTL has not publicly specified the expected ephemeris accuracy for Lunar Pathfinder. We assume the rover acquires ephemerides via the communication link, but both the update cadence and the absolute accuracy of that data are currently unspecified. We therefore reference the Lunar Relay Services Requirements Document (SRD) 3σ requirements for lunar navigation satellites–$13.43\ \mathrm{m}$ in position and $1.2\ \mathrm{mm/s}$ in velocity–as an optimistic bound (NASA, 2022). Assessing the performance under larger ephemeris errors is outside the scope of this work.

3. Simulation Parameters

We initialize the relay orbit to 1 October 2030, 00:00:00 UTC and set the simulation duration to two Lunar Pathfinder periods, or 21.68 hours. The rover's initial position error is set to $100\ \mathrm{m}$ (1σ) per axis in the x, y, and z axes. Doppler measurements are sampled at 1 Hz, and the filter produces a new state estimate every 180 seconds. Performance is assessed over 100 Monte Carlo trials. Table 4 summarizes the simulation settings.

Table 4: Simulation parameters

Parameter	Value
Epoch	2030/10/01 00:00:00 UTC
Simulation duration	$21.68\ \mathrm{hr}$
Initial rover position error (1σ, per-axis)	$100\ \mathrm{m}$
Measurement sampling rate	1 Hz
Filter update interval	$180\ \mathrm{s}$
Batch filter tolerance ε_{tol}	10^{-9}
Monte Carlo trials	100

As our primary metric, let μ denote the mean 3D position error across the 100 Monte Carlo trials. We define the success criterion as achieving $\mu \leq 10\ \mathrm{m}$ within two orbital periods, or 21.68 hours.

V. RESULTS

1. Signal Availability

We define signal availability using two operational criteria: the carrier-to-noise density ratio C/N_0 must be greater than $30\ \mathrm{dB\,Hz}$ and the rover-to-satellite elevation angle must exceed $5°$. Similar metrics for signal availability have also been used in Nardin et al. (2023) and Melman et al. (2022). The C/N_0 threshold reflects a conservative margin for robust carrier tracking, while the elevation mask mitigates low-angle effects. Under these criteria, the rover experiences approximately 3.3 hours of unavailability (or occultation) during each 10.84-hour Lunar Pathfinder orbit (about 30% of the orbital period). For the simulation setup, we select the satellite mean anomaly so that measurement collection begins when the satellite becomes visible. As a result, the occultation intervals are shifted to the final hours of each orbital pass, yielding a contiguous measurement collection window at the start of the scenario. Additional information on elevation, C/N_0, and occultation periods is provided in Coimbra et al. (2024).

2. State Estimation Performance Baseline

As a baseline, we evaluate the state estimation performance for two straight-line rover motion profiles–constant speed and stop–go–under zero velocity noise (i.e., the rover's ground-truth velocity is applied without perturbation). Conceptually, this

benchmark should mirror the stationary case (see Coimbra et al. (2024)) because the rover's displacement from its initial position is perfectly known. Table 5 reports the time required to achieve $\mu \leq 10$ m for each profile.

Table 5: Time to reach $\mu \leq 10\,\mathrm{m}$ for different rover motion profiles

Motion Profile	**Time to achieve $\mu \leq 10$ m [hr]**	
	Mean [hr]	**99$^{\text{th}}$ percentile [hr]**
Stationary (Coimbra et al., 2024)	11.2	15.4
Constant Speed	11.3	16.3
Stop–Go	11.2	15.7

The results are consistent with this expectation: the mean time to meet the accuracy threshold is effectively equivalent across the stationary, constant-speed, and stop–go profiles. The 99$^{\text{th}}$ percentile time is several minutes larger for the moving cases relative to stationary. This difference is attributable to Monte Carlo variability and slight differences in signal availability during rover motion.

3. Rover Motion Model Comparison

The baseline results indicate that, with perfectly known rover velocity, the absolute localization convergence using a single relay satellite is largely insensitive to whether the rover is stationary or in motion. While informative, this assumption is not operationally realistic. As discussed in Section IV.1 b), the stop-go profile is representative of a real proposed mission. In particular, its scheduled stationary periods and cadence can be leveraged to improve localization even when the motion knowledge is imperfect.

Figure 1 compares the position error over time for the constant speed and stop-go rover motion profiles under a 7 $\mathrm{mm/s}$ velocity noise injection to the ground truth (5.0% of the rover's commanded velocity of 0.5 km). The solid blue curve shows the mean across the Monte Carlo trials, the blue shaded band represents the 1σ spread, and the red curve denotes the 99$^{\text{th}}$ percentile. The satellite occultation periods are shown in the shaded gray and the 10 m localization accuracy threshold is shown in the dashed black line. Under these conditions, the constant speed profile reaches the threshold at 14.8 hours, whereas the stop-go profile does so at 13.9 hours, resulting in a reduction of nearly one hour. This improvement arises because the mission-realistic stop-go cadence introduces zero rover motion intervals, which mitigate the impact of velocity errors. In short, planned operational dynamics can be leveraged to improve localization performance in the presence of imperfect motion knowledge.

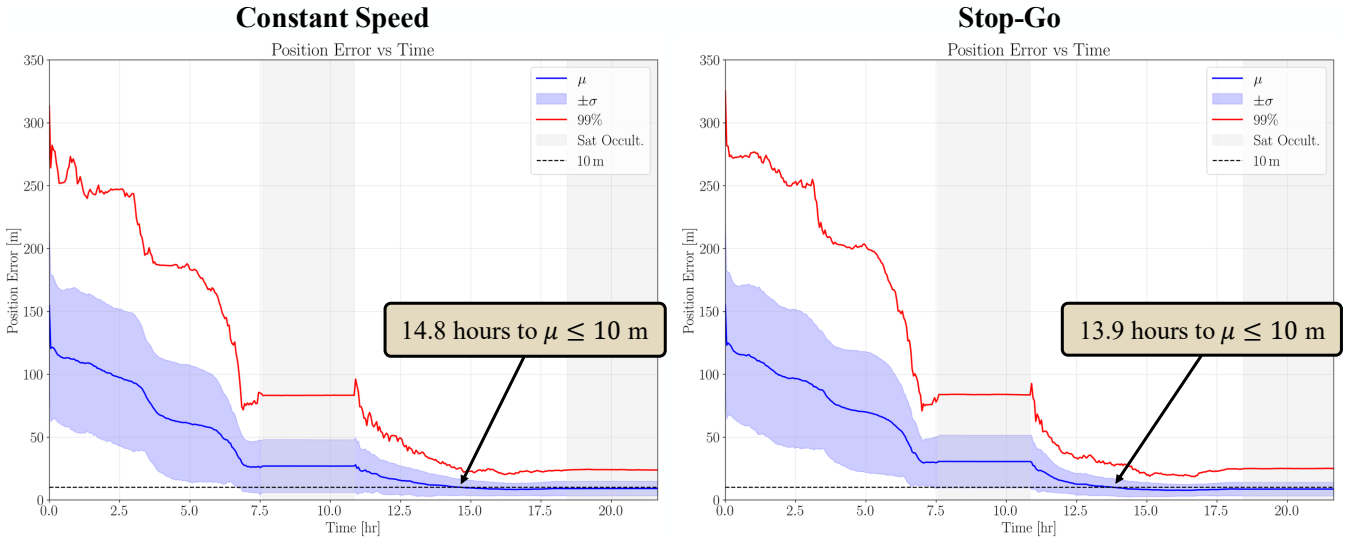

Figure 1: Position error over time for [left] constant speed and [right] stop-go rover motion profiles under a 7 $\mathrm{mm/s}$ velocity noise injection to the ground truth.

4. Sensitivity Study on Rover Velocity Noise

Using the stop-go motion model, we assess the filter's robustness by injecting increasing levels of velocity noise into the rover's ground truth trajectory. Table 6 reports the mean time to achieve the accuracy criterion of $\mu \leq 10$ m as a function of the injected noise level, expressed both in $\mathrm{mm/s}$ and as a percentage of the commanded speed, 0.5 km/hr.

Table 6: Results for increasing levels of velocity noise for the Stop–Go rover motion profile

Velocity noise [mm/s]	**Percent of commanded velocity**	**Mean time to achieve $\mu \leq 10$ m [hr]**
0.0 (baseline)	0.0% (baseline)	11.2
6.0	4.3%	13.3
7.0	5.0%	13.9
8.0	5.8%	14.3
9.0	6.5%	14.9
10.0	7.2%	15.5
11.0	7.9%	> 21.7

The results show a monotonic degradation in convergence time as velocity noise increases: the mean time grows from 11.2 hours with no noise to 15.5 hours at 10.0 mm/s (7.2% of the commanded speed), while still meeting the target within two Lunar Pathfinder orbits (21.68 hours). At 11.0 mm/s (7.9%), the system no longer meets the target within two orbits, indicating a practical limit on the filter's capabilities. Figure 2 shows the position error over time using the maximum applied noise while still maintaining the target (10.0 mm/s). As desired, we see that the position error mostly monotonically decreases over time.

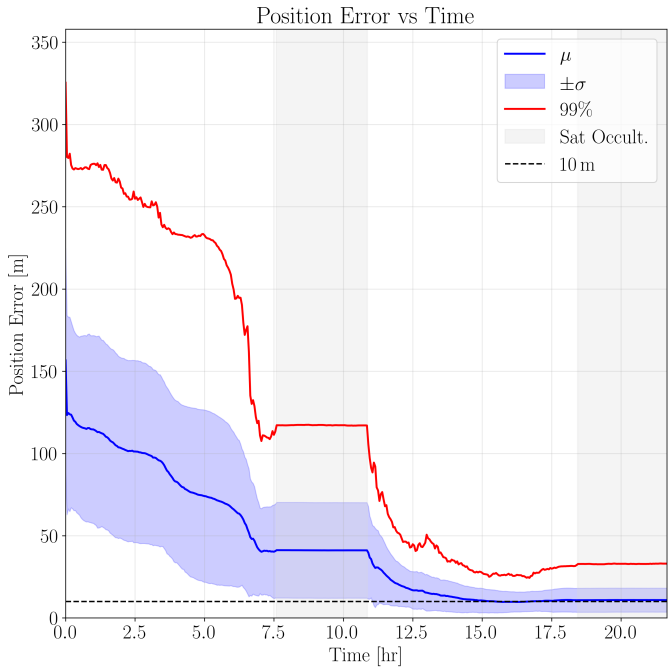

Figure 2: Position error over time with a 10 mm/s rover velocity noise.

Overall, this study quantifies the tolerance of the weighted batch estimator to imperfections in rover-motion knowledge. The findings show that accurate localization remains attainable up to 7.2% velocity error under the stop–go operational cadence, after which performance degrades beyond the two-orbit window.

VI. CONCLUSION

We presented a localization framework for a moving lunar rover that exploits single-satellite measurements without a dedicated navigation payload. The estimator is a weighted batch filter designed for low-observability geometry and mission-realistic operations. To validate the estimator, we used rover dynamics patterned after NASA's Endurance rover mission concept and a relay satellite consistent with ESA's Lunar Pathfinder.

The results show that, with perfectly known motion, convergence to the desired $\mu \leq 10\ \mathrm{m}$ is essentially insensitive to whether the rover is stationary, at constant speed, or following a stop–go schedule. When motion knowledge is imperfect, we find that the mission-representative stop–go cadence is advantageous relative to the constant speed motion profile because the scheduled stops mitigate the impact of velocity errors. A sensitivity study further indicates that sub-10-m accuracy can still be achieved within two Lunar Pathfinder orbits with injected velocity noise up to $10.0\ \mathrm{mm/s}$, or 7.2% of the rover's commanded speed. Beyond this level, the performance degrades and will require a longer duration than the two-orbit window to converge.

Ultimately, this work serves as an initial step toward single-satellite absolute localization for moving surface users. Future work will increase modeling fidelity (e.g., incorporating time-correlated noise processes for measurements and rover motion), examine more challenging rover traverses with turns and speed variations, and integrate additional measurement sources such as IMU, wheel odometry, or multi-satellite support.

ACKNOWLEDGEMENTS

This research is supported by the National Science Foundation (NSF) Graduate Research Fellowship No. DGE-2146755 and the Stanford Knight-Hennessy Scholars graduate fellowship. We would also like to thank the other members of the Stanford Navigation and Autonomous Vehicles Laboratory for their helpful discussions and support.

REFERENCES

Astrolab Venturi (2025). FLEX Rover. https://www.astrolab.space/flex-rover/.

Bhamidipati, S., Mina, T., and Gao, G. (2022). A Case Study Analysis for Designing a Lunar Navigation Satellite System with Time-Transfer from Earth-GPS. *Proceedings of the Institute of Navigation ITM conference (ION ITM 2022)*.

Cauligi, A., Swan, R. M., Ono, H., Daftry, S., Elliot, J., Matthies, L., and Atha, D. (2023). ShadowNav: Crater-Based Localization for Nighttime and Permanently Shadowed Region Lunar Navigation. *2023 IEEE Aerospace Conference*.

Coimbra, K. M. Y., Cortinovis, M., Mina, T., and Gao, G. (2024). Single-Satellite Lunar Navigation via Doppler Shift Observables for the NASA Endurance Mission. *Proceedings of the Institute of Navigation GNSS+ conference (ION GNSS+ 2024)*.

Coimbra, K. M. Y. and Gao, G. (2025). Comparative Analysis and Design of a Dual-Satellite System for Lunar Rover Localization. *2025 IEEE Aerospace Conference*.

Daftry, S., Chen, Z., Cheng, Y., Tepsuporn, S., Khattak, S., and Matthies, L. (2023). LunarNav: Crater-based Localization for Long-range Autonomous Lunar Rover Navigation. *2023 IEEE Aerospace Conference*.

Giordano, P., Swinden, R., Gramling, C., Crenshaw, J., and Ventura-Traveset, J. (2023). LunaNet Position, Navigation, and Timing Services and Signals, Enabling the Future of Lunar Exploration. In *Proceedings of the 36th International Technical Meeting of the Satellite Division of The Institute of Navigation (ION GNSS+ 2023)*, pages 3577–3588, Denver, Colorado.

Jun, W. W. (2023). *Performance of a Low Infrastructure Navigation System for Planetary Surface Users*. Doctoral dissertation, Georgia Institute of Technology, Atlanta, GA, USA.

Keane, J. T., Tikoo, S. M., and Elliot, J. (2022). Endurance: Lunar South Pole-Aitken Basin Traverse and Sample Return Rover. *NASA Jet Propulsion Laboratory, Technical Report*.

Melman, F. T., Zoccarato, P., Orgel, C., Swinden, R., Giordano, P., and Ventura-Traveset, J. (2022). LCNS Positioning of a Lunar Surface Rover Using a DEM-Based Altitude Constraint. *Remote Sensing*, 14(16):3942.

Mizuno, H., Wakabayashi, S., Ohtake, M., Hoshino, T., and Asoh, D. (2024). Development Status in 2024 on Lunar Polar Exploration (LUPEX) Project. In *IAF Space Exploration Symposium—Held at the 75th International Astronautical Congress (IAC 2024)*. International Astronautical Federation (IAF).

Nardin, A., Minetto, A., Guzzi, S., Dovis, F., Konitzer, L., and Parker, J. J. K. (2023). Snapshot Tracking of GNSS Signals in Space: A Case Study at Lunar Distances. *Proceedings of the 36th International Technical Meeting of the Satellite Division of The Institute of Navigation (ION GNSS+ 2023)*, pages 3267–3281.

NASA (2022). Lunar communications relay and navigation systems (LCRNS). *Preliminary Lunar Relay Services Requirements Document (SRD)*.

National Academies of Sciences, Engineering, and Medicine (2023). *Origins, Worlds, and Life: A Decadal Strategy for Planetary Science and Astrobiology 2023-2032*. The National Academies Press, Washington, DC.

O'Dea, A., Kinman, P., Pham, T. T., and Chang, C. (2019). Doppler tracking. *Deep Space Network, DSN No. 810-005, 202, Rev. C*.

Parker, J. J. K. et al. (2025). Initial Results of the Lunar GNSS Receiver Experiment (LuGRE) . *Proceedings of the Institute of Navigation GNSS+ conference (ION GNSS+ 2025)*.

Rabideau, G., Russino, J., Branch, A., Dhamani, N., Vaquero, T. S., Chien, S., de la Croix, J.-P., and Rossi, F. (2025). Planning, scheduling, and execution on the Moon: the CADRE technology demonstration mission. *arXiv preprint arXiv:2502.14803*.

Schmittberger, B. L. and Scherer, D. R. (2020). A Review of Contemporary Atomic Frequency Standards. *arXiv preprint arXiv:2004.09987*.

SSTL (2022). Lunar Pathfinder: Data relay satellite in orbit around the Moon. *SSTL, Service Guide (V4)*.